Light Metals 2008 *Edited by: David H. DeYoung*
TMS (The Minerals, Metals & Materials Society), 2008

HEAT TRANSFER DURING MELT SPINNING OF AL-7%SI ALLOY ON A CU-BE WHEEL

Aravind Sundararajan and Brian G. Thomas
Department of Mechanical Science and Engineering, University of Illinois, 1206 W Green Street, Urbana, IL, 61801, USA
email: bgthomas@uiuc.edu

Keywords: solidification, strip casting, fluid flow, microstructure**,** interface coefficient, aluminum alloys, heat transfer, superheat flux, models, thermocouple measurement

Abstract

Transient heat transfer models of the single-wheel melt-spinning process are developed and applied to quantify the effect of process variables including interface depressions on solidification, temperature evolution, thickness variations, and surface depressions in the cast product. Firstly, a transient one-dimensional heat-transfer model of the melt-spinning process called STRIP1D was developed for Al -7% Si strips on a Cu-Be substrate and validated. Next, transient two- and three-dimensional heat-transfer solidification models of the process were developed and validated using the STRIP1D model. The models have then been used to understand the effect of process conditions including casting speed, puddle length (length of contact zone), gap height, superheat and interfacial depressions (gaps) on heat transfer in the strip, with the help of experimental measurements from a pilot caster in Cornell. The effects of interfacial boron nitride deposits and air gaps were quantified by measuring and modeling longitudinal and transverse surface depressions observed on the wheel-side surface of the strip. Interfacial depressions decrease heat conduction to the wheel and thereby cause surface depressions on the opposite side of the strip. The predicted depression shapes match well with experimental measurements. The control of surface depressions in the melt-spinning process could enable strip casting with imprinted textured surfaces.

I. Introduction

Melt-spinning processes[1, 2] can be used to cast amorphous metallic glass ribbons[3, 4] or thin metal strips[5] with fine microstructure and properties[6-8]. With cooling rates of 10^3-10^6 K/s , this is a rapid solidification process[8]. The strip product can exhibit several different types of observable surface defects [9-11]. These include cracks, holes, hot tears, segregation and surface depressions [9-11]. Steen et al[12-14] have suggested that if the surface depressions can be controlled, this method could be an economical way to produce strip product with textured surfaces embossed with text and images.

Different techniques can be used to produce strips with textured surfaces. These include laser interaction with the melt-pool, meniscus fluctuations from vibrations of the melt pool[6], and treating the wheel surface either thermally (such as via laser scanning) or physically, such as via coating deposits. For example, imprinting a layer of low-conductivity BN onto the wheel can act as an interface surface depression that transfers a ‘negative’ template from the substrate to the product during solidification[13, 14]. Surface depressions include longitudinal depressions along the casting direction and transverse depressions across the width of the strip, as shown in Fig 1(a). A depression on the substrate surface causes a local increase in thermal resistance at the interface between the strip and the wheel (wheel side surface) and thus slows the heat transfer and local solidification rate. This produces a corresponding deeper depression on the opposite upper surface of the strip (liquid side surface) which translates into discernable thickness variations. In order to quantify the effect of these interfacial depressions, a thorough understanding of the heat transfer phenomena occurring during this process is essential.

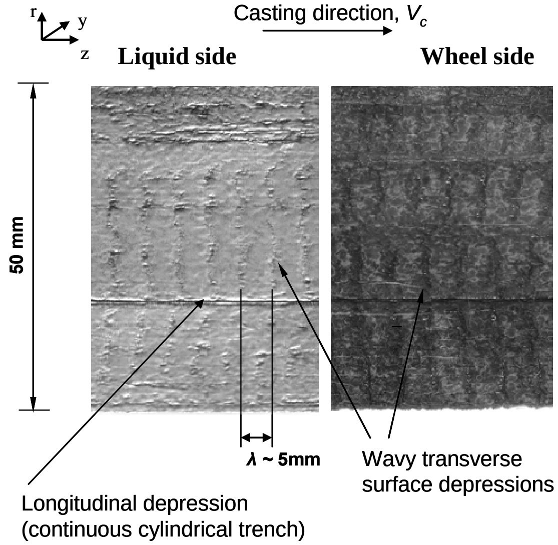

Figure 1 (a) : Depressions observed in strip surface

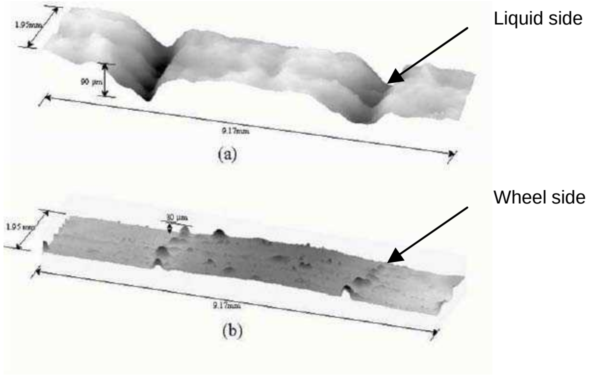

Figure 1 (b): Close up of wavy transverse depressions (Steen et al)

This work focuses on the PFMS process at Cornell University where Al-7% Si alloy is cast into thin 50 mm-wide aluminum strips on a 12.7mm thick, 100mm-wide Cu-Be wheel (substrate). Fig 2 shows a schematic of the process.

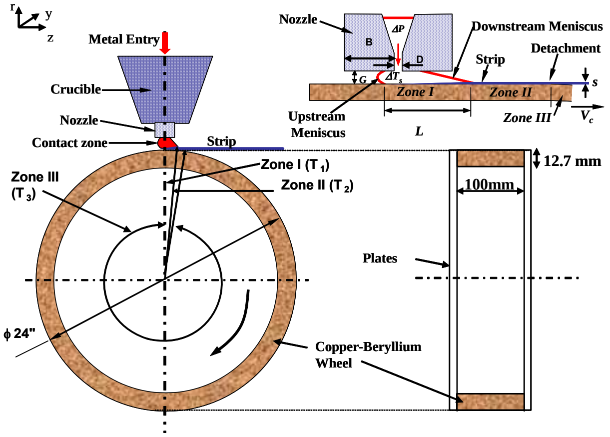

Figure 2. Schematic of Strip Casting Process

Molten aluminum alloy at 714°C (100 K superheat) is poured through the nozzle onto the rotating wheel. As the air-cooled wheel moves, the metal solidifies and detaches in the form of a solidified strip. The thickness *s*, of the ribbons produced ranges from 0.08mm to 0.35 mm[15]. As a first step towards quantitative understanding of heat transfer during melt spinning, a mathematical model of the process called STRIP1D has been developed. STRIP1D is a transient one-dimensional heat-transfer model of the planar-flow melt-spinning process used to cast Al-7% Si strips on a Cu-Be wheel. The STRIP1D model is used to validate two- and three-dimensional heat transfer models of the process. The models are then applied to investigate the effect of casting conditions and interfacial depressions on heat transfer and solidification during melt spinning, including thickness variations and surface depressions. In particular, the longitudinal depressions caused by a continuous ridge of BN deposits and transverse depressions caused by rows of small, closely-spaced air pockets are investigated.

II. Literature Review

Previous work to investigate the strip-casting process includes heat transfer-solidification models of melt spinning, estimating the effects of process conditions[16, 17] on heat transfer in strip casting processes, and understanding the surface defects occurring in different continuous casting processes[9, 11, 18]. Many of the heat transfer models on melt spinning are one-dimensional transient models (of the wheel or of the strip) that have been used to determine average heat transfer coefficients in PFMS. Carpenter and Steen[5] calculated a value of 170 $\mathrm{kW/m^{-2}K^{-1}}$, using one-dimensional Stefan problem of the strip. Kukura and Steen[19] have applied separate uncoupled one-dimensional numerical models of the wheel and strip in PFMS of Al-7% Si and determined an average interface coefficient of 110 $\mathrm{kWm^{-2}K^{-1}}$. They predicted the increase in wheel temperature that arises each cycle. Wang et al[20] developed a 1-D control-volume model of the strip and the wheel to study the effects of undercooling and cooling rate on planar flow casting of aluminum strip on copper. Average heat transfer coefficients of 200 - 1000 kW $\mathrm{m^{-2}\ {}^{\circ}K^{-1}}$ were reported. Hattel and Pryds[21] applied a 1-D control-volume solidification model of melt spinning to find that the delay of initial solidification depends on both the heat transfer coefficient and wheel heating. Including the wheel in the numerical model was found to be essential (even for highly conductive copper), owing to its high surface temperatures. No previous model has coupled the effects of fluid flow and heat transfer in the melt pool with solidification and heat transfer in the strip and transient conduction through the wheel for the melt-spinning process.

Research using calibrated models has investigated the effect of process conditions on heat transfer during the strip casting process. Li and Thomas[16] have computed how increases in casting speed or superheat decrease the strip thickness. An increase in casting speed also increases the average interfacial heat transfer coefficient, thereby increasing the wheel temperature. Muojekwu et al[17] found that the interfacial heat transfer coefficient in aluminum strip casting increases as the wheel roughness decreases, owing to increasing contact between the strip and the wheel. In addition, increasing thermal diffusivity of the substrate material increased the interfacial heat transfer, owing to an increase in the ability of the chill to absorb and transport heat.

Efforts have been undertaken to understand how defects form in the related process of continuous casting of steel. Thomas[22] studied how fluid-flow causes defects to form during solidification. These include excessive surface turbulence causing fluctuations in the surface level, low casting speed or superheat which may result in partial freezing of the meniscus, inclusions and bubbles that may get entrapped in the solidifying shell thereby causing many costly defects in the final product. Sengupta et al[23] have found the formation mechanism of hook-type oscillation marks, which are long transverse depressions in the surface of the solidifying steel. They initiate by partial meniscus solidification, and the instantaneous shape of the meniscus at this time dictates the shape of the defect and its microstructure. The spacing of these marks is the product of the casting speed and the period of the mold oscillation cycle. Singh and Blazek[24] observed that solidifying shell is rippled for peritectic steels. The oscillation marks for these compositions are deeper. Jenkins and Thomas[25] have confirmed that deep surface depressions are responsible for the local variations in thickness of the steel shell. Thomas et al[26] have quantified the effect of an oscillation mark on decreasing interfacial heat transfer which delays the local solidification rate and results in a thinner steel shell. Level fluctuations are deviations of the meniscus position at the mold wall, which also lead to non-uniform solidification, deep oscillation marks, and surface cracks. Kubota[27] and Sasabe[28] found that large level fluctuations correlate with defects in the steel product.

There have been attempts to classify the defects occurring in melt-spinning. Depressions occurring at the liquid side surface of the strip form due to differential heat transfer from depressions at the wheel side, or due to unsteady fluid flow in the melt pool[9, 29]. Legresey et al[29] have attributed transverse thickness variations (longitudinal depressions) to heat-transfer variations at the strip-wheel interface and longitudinal thickness variations (transverse depressions) to fluctuations of the liquid metal level in the crucible. Carpenter and Steen[9] classified the most common surface defects in the planar-flow spin-casting process as dimples, streaks, herringbone and cross-stream patterns[6]. The dimple pattern is the most common type of defect in pure aluminum. Each dimple is a depression on the liquid side surface of the strip that corresponds with a small depression at the same location on the wheel side surface of the strip. The streak pattern appears as long thin grooves that usually run along the casting direction (longitudinal) on the upper surface of the strip. Both the dimple and steak pattern depressions have been suggested to occur due to small gas pockets on the wheel side that form by air entrainment when the liquid metal first contacts the wheel[9]. Each pocket retards the heat transfer locally, so solidification is slower than elsewhere in the strip, which results in a depression on the liquid side of the strip. The herringbone pattern found on the wheel side of the strip, consists of wavy transverse lines on the wheel side and is caused by non-uniformities in fluid-flow. A small piece of metal protruding into the nozzle induces non-uniform flow and generates this pattern on the strip surface. Although the herringbone pattern consists of liquid side depressions similar to the other patterns, it suppresses other instabilities so the surface is smoother than with the streak or dimple patterns[9]. The cross-stream pattern is similar to the herringbone pattern and occurs only in alloys such as Al-7%Si. The pitch between the herringbone defects is ~1mm,[9] and between successive cross-stream waves (depressions) is ~ 8mm, which matches with the oscillation frequency of the liquid pool[6].

It is clear from previous work that fluid flow is responsible for transverse depressions and the herringbone and cross-stream patterns. It is not clear, however, if the waves caused by the time-dependent flow freeze to form surface depressions directly, or act indirectly by affecting the upstream meniscus. Despite many previous studies of surface defects in melt spinning, there has been very little effort to quantify them. This paper aims to develop multi-dimensional heat-transfer models of the process and use them to quantify the effect of wheel-side surface depressions and other casting parameters on heat transfer and upper-surface depressions and thereby confirm the mechanism of their occurrence.

III. Analysis of Strip Casting Experiments

The model development and investigation of the effect of process variables on the heat transfer and surface defects during the melt-spinning process was done with the help of five different casting experiments performed with the pilot caster at Cornell University[30]. A complete set of conditions and results were recorded as a function of time during each run, including casting speed, puddle length, gap height, strip thickness, and wheel temperature. Puddle length was measured using a high-resolution video recording shot during the cast. The solidified aluminum strip was cut into 15-cm long pieces and the average thickness of each sample was calculated by dividing its mass by the density, width, and length. Process conditions of several cases are given in Table 1.

To investigate interfacial surface depressions, special attention was focused on Case 43, (Cast ID ODSU06_43)[31] which contained two different types of surface defect, pictured in Fig 1(a). The first type was a long, continuous longitudinal depression, created by spraying a ridge of boron nitride onto the wheel surface prior to casting. The ridge was a straight line of about 0.03-mm high and 0.25-mm wide, consisting of many overlapping spot deposits. The second type was a cross-stream pattern, which appeared as a series of transverse depressions (see Fig 1(a)). The depressions are continuous cylindrical trenches that form roughly parallel wavy lines across the strip. Each depression corresponds exactly with a line of very closely spaced craters across the width of the strip on the wheel side. Fig 1(b) shows a close up of two rows of transverse depressions and reveals very small transverse air pockets, about 0.03 mm deep. Although these pockets appear hemispherical, others are about 3-5 times longer than their width, with a depth similar to their width. Note that the surface also includes random pockets that do not align to produce a transverse depression.

In order to measure these depressions, representative sections of the strip containing each type of depression were cut out and mounted in epoxy resin. The cylindrical samples were polished to 1200μm carbimet paper and 0.3μm alumina powder solution, and photographed. The micrographs were measured to obtain accurate local strip thickness and dimensions of the surface depressions.

IV. Melt-Pool Model

The metal delivery system affects the melt-spinning process, by controlling the mass flow rate, and delivery of superheat. The first part of the current model simulates fluid flow and heat transfer in the melt pool (Zone I). In addition to understanding the flow dynamics, this model is needed to obtain the heat flux profile applied on the solid-liquid interface of the STRIP1D model in order to account for the superheat entering the solidifying strip from the liquid metal.

A. *Model Description*

A two-dimensional steady-state fluid-flow and heat-transfer model was used to obtain the velocity and temperature distribution in the liquid pool by solving the Navier Stokes equations, k-ε turbulence model, and energy balance equations using the SIMPLE finite-volume algorithm with FLUENT. The domain includes the entire length and shape of the liquid pool, which was measured from a video recording of the process. The domain, process, and boundary conditions are shown in Fig. 3(a) and Table 1.

Liquid aluminum enters the pool with a velocity of 0.97 m/s at a pour temperature of 714°C (T_{pour}). The top surface (ceramic wall) of the domain was assumed to be flat with a no slip boundary condition at a constant temperature of 714 °C, owing to continuous contact of the refractory nozzle with the melt. The bottom surface of the domain is the interface between the liquid and the solidification mushy zone. It is maintained at the liquidus temperature of 614 °C (T_{liq}) and moves at a constant speed of 7.02 m/s (v_z) in the casting (z) direction. A free slip condition with convection heat transfer coefficient of 10W/m^{2}K was imposed on the free surfaces exposed to the atmosphere.

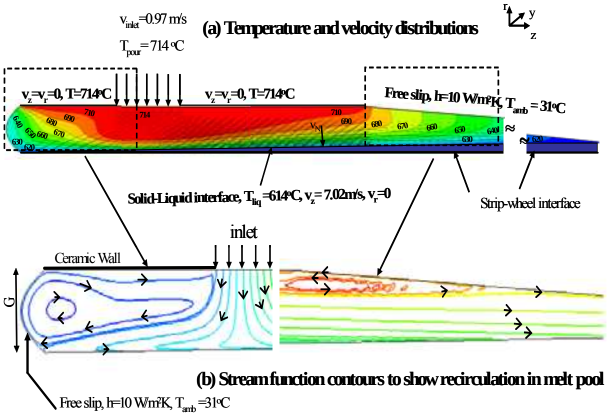

Figure 3. Fluid-flow model velocity and temperature distribution in melt pool – (Case 43)

B. *Model Results*

A typical velocity distribution is included in Fig 3(a). The velocity is maximum at the interface and decreases rapidly with distance into the puddle. Fig 3(b) shows the stream function contours which reveal the recirculation zones. Small recirculation regions are observed on both the left and right of the inlet jet. The fluid enters the domain vertically downwards, impinges on the strip and splits. One jet moves towards the left (against the casting direction) and re-circulates back into the pool. As the other jet travels towards the right free surface, its recirculation disappears at around 7mm along the puddle length, whereupon the flow is all in the casting direction. The velocity profile decreases uniformly from the strip towards the free surface. This type of re-circulating flow pattern is typical of melt-pool models[4, 32] In actuality, the free surface oscillates due to the turbulent flow, with a frequency that is proportional to the flow rate[15].

The temperature distribution observed in the liquid pool is shown in Fig 3(a). Temperature contours naturally follow the fluid-flow pattern. As expected, a steep temperature gradient is observed near the interface. There is negligible heat gained from conduction from the upper nozzle walls, or heat lost due to radiation away from the surfaces exposed to the atmosphere. The steepest, gradients are found directly beneath the nozzle owing to the hot liquid jet entering the domain. Thus, the superheat flux to the strip is a maximum at the jet impingement point, and decreases with distance on either side.

Fig 4 shows the heat flux profile output along the interface between the liquid and the solidification mushy zone. This heat flux profile is input as superheat flux into the STRIP1D Model which is discussed in the next section. The superheat flux is a direct function of casting speed[33], superheat temperature[33], and strip thickness. Assuming that the curve shape is relatively independent of puddle length, the effect of changes to these four casting conditions on the superheat flux have been incorporated[34]. This can be used to obtain the fluid flow results for other cases for STRIP1D can be estimated without re-running the fluid-flow model. Fig 4 compares the superheat flux profiles obtained for a thinner strip (0.168mm) using the melt-pool model and with the relation[34] using standard flow simulation results for 0.215mm strip. The heat flux from the actual simulation is higher near the impingement point and lower near the end of the puddle. However, the total area under both curves is the same, so the total heat entering the interface is the same in both cases.

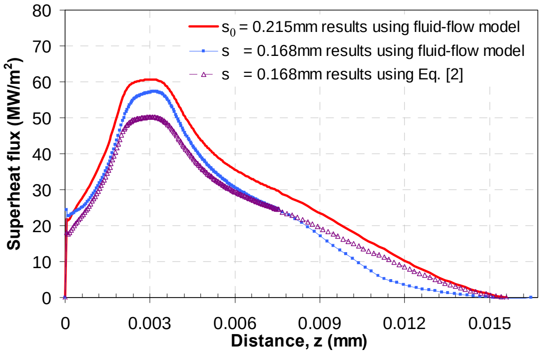

Figure 4: Superheat flux profiles

V. Heat-Transfer Solidification Models

A thorough understanding of heat transfer in the melt-spinning process requires accurate computational models. The transient one-dimensional heat-transfer model STRIP1D[34] was applied to simulate the strip, interface and wheel. A separate two-dimensional steady model of fluid-flow and heat transfer has been developed of the liquid pool (zone I) with FLUENT[36] to obtain the superheat flux profile at the solidification front. The model features a time-dependent heat-transfer coefficient at the strip-wheel interface. Transient two- and three-dimensional heat-transfer models have been developed using ABAQUS[35].

The initial wheel temperature (T_{winit}) and the ambient temperature (T_{amb}) of 31.7°C was taken from experimental measurements. A constant density of 2400 kg/m^3, thermal conductivity of 135 W/m K and specific heat of 1190 J/kg K are used for Al-7% Si[34]. The average casting speed, puddle length, and other variables are taken from experimental measurements, given for several cases in Table 1.

A. STRIP1D Model: STRIP1D is a one-dimensional transient heat-transfer model that solves the following Fourier heat conduction equation[37].

$$\rho c_p \frac{\partial T}{\partial t} = k\frac{\partial^2 T}{\partial r^2} + \frac{k}{r}\frac{\partial T}{\partial r} + \frac{\partial k}{\partial t}\left(\frac{\partial T}{\partial r}\right)^2 + Q \qquad (1)$$

This finite-difference model follows the transient temperature evolution of a one-dimensional slice domain through the strip, and the wheel beneath it, along the casting direction in a Lagrangian frame. Fig 5 shows this model domain and the boundary conditions used. The following assumptions have been used to simplify the model.

- The process is at steady state, including the fluid-flow pattern and resulting superheat distribution along the solidification front.
- There is no relative motion between the strip and wheel
- Heat loss across the width of the strip (y direction as in Fig 2) is negligible
- Circumferential heat conduction in both the wheel and strip along the casting direction is negligible, as the Peclet number, Pe, is large.
- Strip thickness remains the same after it exits the liquid puddle at the end of zone I.
- The mushy zone moves with the wheel at the casting speed without any change in shape.

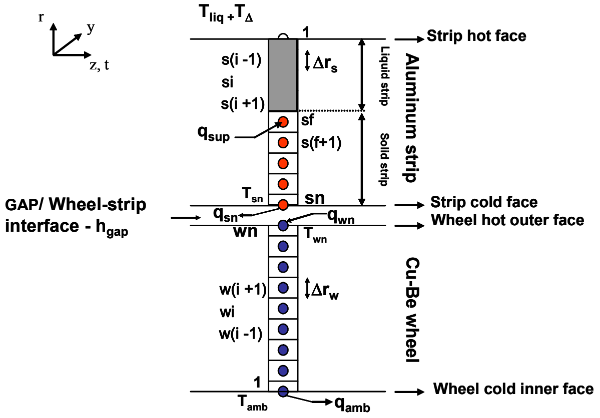

Figure 5. 1-D slice domain of STRIP1D model

Eq. (1) is discretized using an explicit formulation, with a time step, Δt, of the order of 10^{-9} sec and mesh spacing in the strip, Δr of 1μm. The wheel is divided into three zones according to θ in Fig 2. Zone I is the region where liquid is in contact with strip, so is also known as the "puddle region". In Zone II the solidified strip cools in contact with the wheel and Zone III is after they separate. The boundary conditions in each zone are summarized below for the strip and wheel. A typical simulation of 10 wheel revolutions (2.7s real time) takes 20 min on a Intel Xenon 2.6 GHz PC for a time step size of 10^{-9}s (zone I-II) and 10^{-6}s (zone III) for 250 nodes in the strip and 200 nodes in the wheel.

Zone I (puddle region): In this zone, the solidifying strip moves through the melt pool while in contact with the wheel.

Strip: The melt-pool model described in section IV is used to obtain the superheat flux distribution at the interface between the liquid and the solidification mushy zone. The solidification front location, s, is determined at any instant, by the following linear interpolation. The liquidus temperature, T_{liq}, was used as the criterion to define the solidification front in the melt-pool, determined by the solid fraction $f_s(0)$.

A new time- and gap-thickness-dependent thermal convection boundary condition has been applied at the strip-wheel interface.

$$-k_s \left.\frac{\partial T}{\partial r}\right|_{r=r_0} = q_{sn} = -q_{wn} = h_{gap}(T_{sn} - T_{wn}) \tag{2}$$

where h_{gap} is given by

$$h_{gap} = \left\{ \begin{array}{cc} h_0 & t \le 10^{-4} \\ h_0 \left(\dfrac{10^{-4}}{t} \right)^{\frac{1}{3}} & t_{\det ach} > t > 10^{-4} \end{array} \right\} \tag{3}$$

and h_0 is given by

$$h_0 = 225G \tag{4}$$

Wheel: The hot outer surface of the wheel experiences convective heat transfer given by Eq. (2) at the interface and the cold inner surface is exposed to ambient cooling:

$$q_{amb} = h_{amb}(T_{w1} - T_{amb}) \tag{5}$$

Where T_{w1} is the temperature at the inner surface of the wheel. The ambient heat transfer coefficient (h_{amb}) of 25W/m^{2}K has been estimated using the empirical relation established for flow over a cylinder[38]. Also taken into account is heat loss Q_{sides} from the wheel sides due to convection. This is done by treating the convective heat transfer as a volumetric heat source removal from within the wheel.

Zone II (Strip cooling zone): In this zone, the mushy or solidified strip is outside the melt pool but still in good contact with the wheel. Thus, this region employs the same function for heat transfer coefficient h_{gap} for q_{sn} or q_{wn} as in Zone I at the wheel-strip interface given by Eq (2). Zone II ends when the strip becomes fully solid and thereby gains the necessary strength to break off from the wheel, due to mismatching thermal strains.

Strip: The strip is outside the liquid pool so its thickness is constant and its upper surface is exposed to ambient cooling

$$q_{sf} = (h_{amb} + h_{rad,sf})(T_{sf} - T_{amb}) \tag{6}$$

Wheel: The wheel experiences the same boundary conditions as in Zone I given by Eqs. (2) and (5).

Zone III (Non-contact Zone): After exiting Zone II, the parts of the domain representing the solid strip and the wheel are mathematically separated. Thus, this zone consists of the rest of the wheel and the detached portion of the strip.

Strip: The detached strip is exposed to the atmosphere on both sides, where forced convection and radiation are applied:

$$q_{sn} = (h_{amb} + h_{rad,sn})(T_{sn} - T_{amb}) \tag{7}$$

$$q_{sf} = (h_{amb} + h_{rad,sf})(T_{sf} - T_{amb}) \tag{8}$$

where, $h_{rad,sn} = \varepsilon\sigma_{SB}\,(T_{sn}^2+T_{amb}^2)(T_{sn}+T_{amb})$ and $h_{rad,sf} = \varepsilon\sigma_{SB}\,(T_{sf}^2+T_{amb}^2)(T_{sf}+T_{amb})$.

Wheel: Both surfaces of the wheel undergo ambient cooling.

The complete history of a slice through the strip is simulated once each wheel revolution. The simulation continues for any desired number of cycles, during which the wheel continuously heats up.

B. 2-D Model: Multi-dimensional models are required to predict the effect of wheel side depressions and ridges on the strip surface.Fig 1(a) shows a typical longitudinal depression in the strip running along the casting direction. Since the depressions on both sides of the strip can be considered as long continuous cylindrical trenches, a 2-D transverse slice through the depression is sufficient to accurately predict the shape of the liquid side depression. Ignoring the wheel curvature effects, the 2-D transient heat conduction equation in Cartesian coordinates (r, y) governing this process is:

$$\rho c_p \frac{\partial T}{\partial t} = k\left[\frac{\partial^2 T}{\partial r^2} + \frac{\partial^2 T}{\partial y^2}\right] + Q \tag{9}$$

Fig 6 (a) shows the 2-D domain and boundary conditions used. The wheel-side depression is modeled as a part of the domain with properties of the material in the depression. The liquid side depression is inside the domain, which is assigned properties of Al -7% Si throughout. Its shape is defined by the liquidus contour at the exit of Zone I. The equations are solved using a 0.001 x 0.001mm mesh of 4-nodes linear elements in ABAQUS[35].

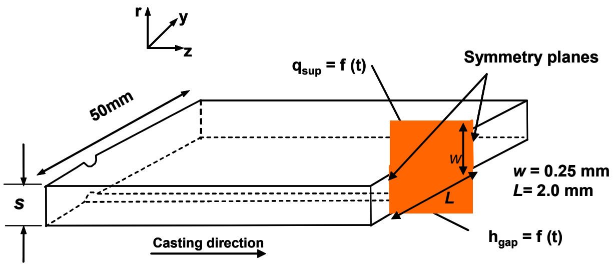

Figure 6(a): **2-D Model domain and boundary conditions for simulating longitudinal depressions**

The bottom surface of the domain forms the strip-wheel interface and is exposed to convective heat transfer with the wheel, with a time-dependent heat transfer coefficient. The STRIP1D model was run using the same simulation conditions to obtain the wheel temperatures which are input to ABAQUS at the strip-wheel interface. The superheat flux obtained from the fluid-flow model described in section IV is input to the top surface of the domain. In the STRIP1D model this heat flux is added at the node just below the liquidus temperature (T_{liq}) which forms the interface between the liquid and solidifying mush. However, in the ABAQUS model these internal nodes cannot be accessed, so the superheat flux curve was added along the top surface of the domain. Because conduction through the liquid changes the superheat flux reaching the internal interface, the superheat flux input to the 2-D ABAQUS model had to be adjusted in order to match the solidification front growth profile obtained from STRIP1D. This was done by increasing the superheat by 150% before the impingement point, by 10% at the impingement point, then dropping it by 50% for a distance of 0.008m then finally increasing by 50% for the rest of the distance in Zone I. This resulted in a net increase of superheat by 74% over that obtained from the fluid-flow simulations, which went to provide sensible heat to the extra liquid elements in the 2-D model. Because of symmetry, both vertical sides of the domain were insulated. Like in the STRIP1D model, the whole domain is given an initial temperature of T_{liq} + T_{Δ} in order to avoid numerical errors owing to inaccurate interpolation.

C. Extension to 3-D Model: Fig 1 (b) shows a close up of typical transverse surface depressions which occur as hemispherical craters. The actual sample modeled here had elongated craters, with 0.046mm width, 0.023mm depth and 0.3 mm length that were spaced about every 0.1mm along the width and 5mm along the length of the strip. Unlike the long continuous trenches in the previous case, these depressions require solving the heat conduction equation in all three coordinate directions, in order to accurately simulate their effect on the heat transfer. Fig 6(b) shows the model domain and boundary conditions. Exploiting periodic symmetry, a domain of 0.05 x 2.5mm is chosen to simulate one quarter of one crater and the corresponding strip, along with a domain height of 0.25 mm.

The boundary conditions are extended from the 2-D model case. An important difference is that the heat transfer coefficient h_{gap} and the superheat flux q_{sup} along the bottom and top surfaces respectively are transformed into functions of both time t and position z in order to convert the Eulerian reference frame to the Lagrangian frame of the model. This means that h_{gap} and q_{sup} vary along the casting direction as every point along the length of the domain has a different value of h_{gap} and q_{sup} as boundary conditions at a given time. The local time t_{local} at any given distance z along the domain from the right edge is given by:

$$t_{local} = t(\mathrm{sec}) - 10^{-3} z(mm)/V_c(m/s) \tag{10}$$

where V_c is the casting speed, and t is the time measured from when the right (front) edge of the domain is at the meniscus. The heat transfer coefficient at any point along the domain length is given by combining Eqs. (3), (4), and (10):

$$h_{gap}(z,t)(kW/m^2K) = 225G(mm)\left(\frac{10^{-4}}{t_{local}}\right)^{0.33}, \tag{11}$$

$$t_{local} > 10^{-4}$$

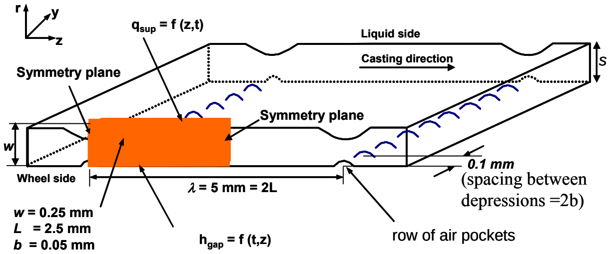

Figure 6 (b): 3-D Model domain and boundary conditions for simulating transverse depressions

VI. Model Validation

As discussed in Section IV, the melt-pool model is used to obtain the superheat flux profile along the interface between the liquid and the solidification mushy zone. This profile is input into STRIP1D to incorporate the effect of the superheat on the strip temperature evolution and solidification, instead of letting the superheat simply conduct through the liquid. The superheat flux can be treated like an internal heat flux boundary as applied in previous work[37]. In the "superheat flux method" of the current work, superheat flux was treated as a heat source added to the closest node below an internal insulated interface (liquidus temperature). The initial temperature of the domain is dropped to $T_{liq}+T_{\Delta}$, so that superheat is taken into account only by the imposed superheat flux profile. Using the theoretically best value of T_{Δ} of 0.0 has the undesirable numerical consequence of inaccurate interpolation of the position of the solidification front. A post-iterative correction is finally made to all nodal temperatures above the liquidus temperature by reassigning them back to $T_{liq}+T_{\Delta}$,. A value of 3. for T_{Δ} was found be the most appropriate choice.

In order to validate this method, a simple "validation case" was performed with conditions listed in Table 1, and also compared with results using ABAQUS. The fluid-flow model, was simplified to constant initial temperature (T = 714^{o}C) fluid moving with the strip along z direction at a constant velocity (6.23 m/s). This is equivalent to the assumptions made with a transient model (ABAQUS or STRIP1D) formulated in a Lagrangian frame with simple conduction through the superheated liquid. Using a fixed temperature (614^{o}C) lower boundary condition, the superheat flux crossing the liquid-mush interface to enter the strip calculated using FLUENT for this case was obtained. Transient conduction simulations were then performed with both STRIP1D and ABAQUS using a domain height of 1.5mm. Results using both constant thermo-physical properties and realistic temperature-dependent properties for this alloy[39] were compared and validated[34] using ABAQUS.

A match in the solidification front growth profiles was obtained from STRIP1D using the superheat flux method and the simple conduction method. The superheat flux method generates the same strip growth profile for different domain heights, ranging from 0.25 to 1.5 mm. Also, a near-perfect match in the temperature distribution through the thickness of the strip at specific times for the STRIP1D and ABAQUS models using either the simple conduction or the superheat flux methods was observed. The superheat flux method fixes temperatures in the liquid to just above the liquidus temperature ($T_{liq}+T_{\Delta}$), so are not expected to match the simple conduction method in the liquid where the initial temperature is T_{pour}. These results demonstrate that the superheat flux method is valid and can be used to couple the effect of fluid flow in the melt pool with heat transfer in the strip and wheel.

This "validation case" explained above was then extended to 2-D. The right edge of the 2-D domain in Fig 6 (a) in section V B opposite from the wheel-side depression is equivalent to the one-dimensional domain in STRIP1D. The model simulates the strip in zones I and II. In zone I, the heat flux curve obtained from the results of a fluid-flow heat-transfer model of the melt-pool in FLUENT, is imposed on the top surface to account for the superheat flux entering the solidifying shell. The wheel side is exposed to convective cooling at the strip-wheel interface as in STRIP1D. The vertical sides of the domain were insulated owing to symmetry. As with STRIP1D, the initial temperature is 617^{o}C, which includes T_{Δ} = 3 ^{o}C to avoid numerical errors. The domain height is dropped to 0.25mm to minimize errors from conduction in the liquid. The simulation conditions are given in Table 1.

Reasonable agreement in the solidification front growth profiles between the STRIP1D and ABAQUS models for these conditions was observed[34, 40]. The ABAQUS model profile is slightly higher than the STRIP1D model in the initial 1.7 ms, due to adding the superheat to the top surface and not at the interface. Temperature evolution through the strip thickness was also compared and a perfect match is observed. Only temperatures in the solidifying strip are comparable, as temperature evolution in the liquid is not modeled accurately with the superheat flux method. The 2-D model is further validated by comparing solidification front and temperature predictions in zone II, as explained in section VIII E1. The 3-D model is validated in a similar manner by comparison with STRIP1D predictions far from the depressions. This is discussed in section VIII E2.

VII. Typical Results

The STRIP1D model thus calibrated has been validated with experiments conducted at Cornell University[41]. Case 43 (Cast ID # ODSU06_43) was chosen to verify the model predictions. The experimentally observed trends for the gap height, G with time of cast, t in Fig 7 were used to vary the heat transfer coefficient with gap height using Eq. (4).

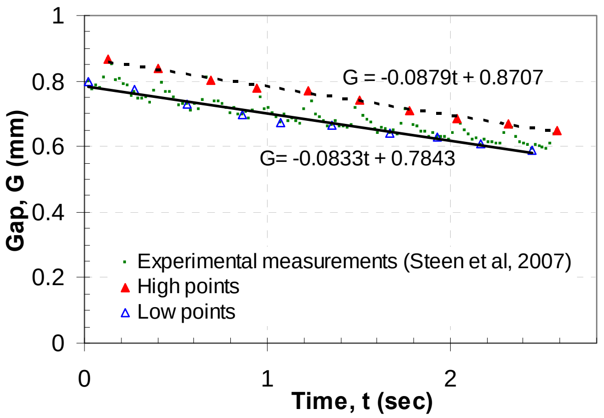

Figure 7: Measured Gap height history – (Case 43)

Owing to fluctuations in the observed data, two sets of gap data, highs and lows of the data points, were chosen and a line of fit was drawn through each to define G variation with time.

A. Solidification front growth: The predicted solidification front profile in Zones I & II is shown in Fig 8. Without undercooling, solidification starts at 1µs and increases rapidly. The predicted front growth slows beneath the jet impingement region, and then increases sharply as the superheat diminishes. The temperature contours for different solid fractions in the strip have a similar steep shape and are almost parallel to each other. This logical but nontraditional profile agrees with the solidification front growth reported by Chen et al[42]. The liquidus reaches the top surface in 2.36 ms from the start of contact at the meniscus, and the solidus after 13.6 ms. This long delay is due to the lower heat transfer rates predicted at greater times by Eq (3). The extensive mushy region is predicted to persist well past the end of the liquid pool. The strip is proposed to detach from the wheel (end of Zone II) at ~87mm when it fully becomes solid and gains the necessary strength to break off from the substrate surface.

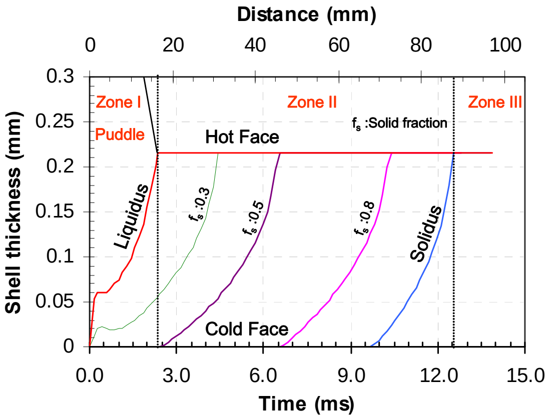

Figure 8: Solidification front growth

B. Strip thickness: Fig 9 shows excellent agreement in the strip thickness between the model predictions and the experimental observations[41] and captures the observed variations in two different time scales.

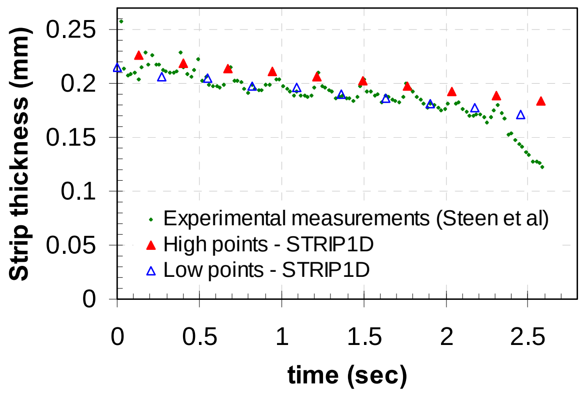

Figure 9: Measured & Predicted strip thickness history – (Case 43)

The overall decreasing trend in strip thickness profile can be attributed to two main reasons. Firstly, because the gap height generally decreases with time, the heat transfer coefficient decreases from Eq. (4). Secondly, because the wheel temperature increases each cycle, less heat flux is extracted (from Eq. (2)). A third minor contributing reason is the decrease in puddle length with time, which is caused by flow resistance associated with the decreased gap. This shortens the time available for solidification, so tends to decrease the strip thickness. However, after cycle 4, the puddle length remains almost constant while the strip thickness drops significantly. The effect of puddle length is incorporated in the predictions, but turns out to be small.

It is interesting to note periodic glitches in the measured strip thickness within each cycle, which are represented by selected high and low points. These are caused mainly by the periodic variations in measured gap height (Fig 7) owing to the slightly oblong wheel shape. Bulges on the wheel form a low measured gap beneath the nozzle and the depressions form a high gap. According to Eq. (4), the heat transfer coefficient varies and generates a similar trend in the observed strip-thickness profile. Again, the measured puddle length also drops from high to low points, but its effect is less important.

The predictions do not match well with the thicknesses measured during the start and end of the process. This is because the empirical relation developed between the gap height and the heat transfer coefficient does not hold well during these times. Once the process begins, it takes some time for it to stabilize and reach steady state. During the end of the casting process, the pressure head of the melt in the crucible drops, which lowers the liquid flow rate, and decreases the strip thickness, in order to satisfy the mass balance. However, this is accompanied by an increase in the measured puddle length, so the interfacial heat transfer must drop, in order to satisfy the heat balance. This might be due to chaotic flow variations, wheel surface contamination, or other reasons.

C. Solidification velocity, cooling rate, and microstructure: The velocity of the solidification fronts is simply the average slope of the liquidus and solidus lines in Fig 8. Velocities of 0.082 m/s (liquidus) and 0.078 m/s (solidus) lie within the range of 0.05 -0.1 m/s reported by Byrne et al[6]. The liquidus grows at a faster rate than the solidus because the heat transfer coefficient decreases along the casting direction according to Eq. (3).

The time difference between solidus and liquidus from Fig 8 was used to obtain the solidification time t_{sol} at various thicknesses through the strip. The obtained solidification time t_{sol} can be used to determine the cooling rate (CR) by

$$CR = \frac{(T_{liq} - T_{sol})}{t_{sol}} \qquad (12)$$

The top surface and interface have similar cooling rates, owing to the high conductivity and thin strip of this process. The predicted cooling rates of 5800-6000 deg/sec are on the same order as the average cooling rates reported by Byrne[30] using Bamberger's model[43].

The solidification times can also be used to predict the SDAS of the microstructure, λ, using an empirical relation developed by Spinelli[44].

$$\lambda = 5(4.9 t_{sol})^{0.333} \qquad (13)$$

Fig 10 compares the predicted and measured SDAS at various locations through the strip. Because the conditions of the experiments were different[30], and the model does not take into account the nonlinear dependency of latent heat on the solid fraction, a perfect match between SDAS predictions and measurements is not expected.

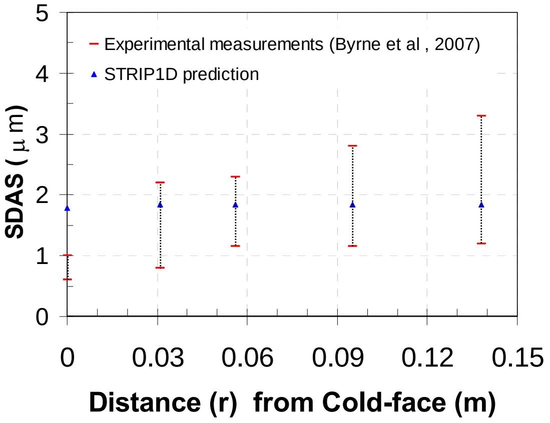

Figure 10: Measured and predicted SDAS through the strip thickness (Case 43)

D. Strip surface temperatures: Fig 11 shows the temperature history at the strip hot and cold faces. The predicted cold-face surface temperature profile has a small dip in zone I. This indicates reheating, but is not due to either nucleation undercooling[45] or sudden drops in interfacial heat flux[46] which have been observed in other work. Here, the reheating is attributed to the peak superheat flux at the region of jet impingement, as discussed in section VII A.

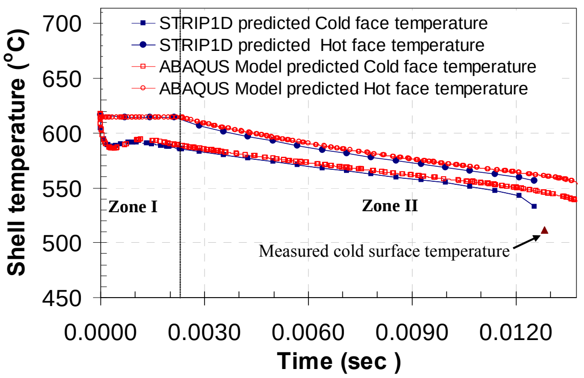

Figure 11: Strip surface temperature profiles (Case 43)

The predicted strip hot and cold face temperature profile is in great agreement with that obtained from the ABAQUS model. It is clear that the predicted cold face temperature of the strip at the exit of zone II (detachment) of 537°C is within 5% of the experimentally measured exit temperature of 512°C. The prediction is expected to be higher because the exit temperature can be experimentally measured only after a few seconds after the strip leaves the wheel. Fig 12 shows the temperature through the thickness of the strip at various times in Zones I and II. Temperature gradients through the strip thickness are relatively small, as the center cools within 20°C of the surface after only 13.6ms.

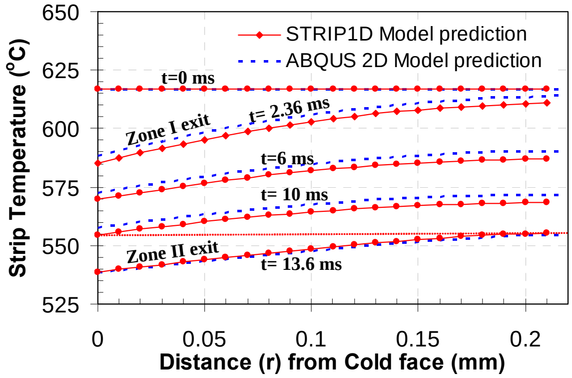

Figure 12: Predicted temperature profile through shell thickness over time (Case 43)

E. Heat Balance: A detailed heat balance for cycle 3 of this simulation, case 43 was obtained. The total heat flux extracted from the strip (and entering the wheel) is calculated by integrating Eq. (2) until the end of zone II. This total heat flux is the sum of the superheat, latent heat and the sensible heat. The latent heat comprises around 68% of the total while the superheat and sensible heat contribute 20% and 12% respectively. These fractions are consistent with other work on strip casting[16, 19]. Owing to numerical errors, the sum of these three parts is 3% more than the total, which indicates the accuracy of the computation.

.

F. Wheel temperatures: To evaluate the wheel temperature predictions, the temperature profile 2mm below the wheel surface was used to predict the thermocouple temperature with the aid of an additional model of the thermocouple[34]. The results in Fig 13 show excellent agreement with the experimental measurements for all ten casting cycles.

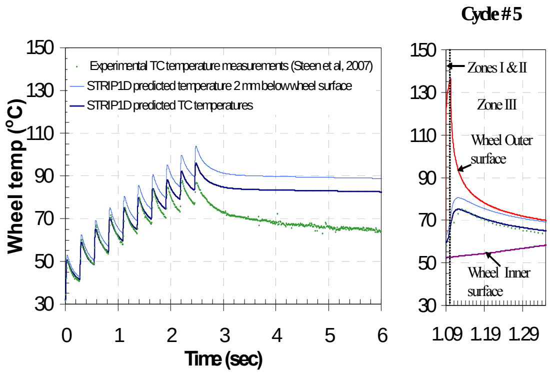

Figure 13: Measured & Predicted wheel TC temperature history (Case 43)

The wheel heats up each cycle and never reaches steady state. The hot face where heat is input naturally reaches high temperatures very fast. Heat is extracted from the strip mainly by the cold thermal mass of the wheel, which heats up monotonically only a little each cycle. The increase in wheel temperature decreases with each passing cycle because the initial heat transfer coefficient h_0, decreases with cycle owing to the general decrease in gap height during the cast. Because air cooling of the wheel is very small, there is a limit to the number of cycles possible before the wheel becomes too hot to solidify any strip.

The STRIP1D-predicted wheel temperatures match well with the measurements while the strip is contact with the wheel. During this time, there are steep temperature gradients in the wheel and only the surface layer of the wheel is heated (see Fig 13). The wheel acts almost like a semi-infinite domain and its thickness is not very important. Once there is no more metal-substrate contact, however, internal temperature gradients subside as the wheel undergoes only ambient cooling. The predicted temperature no longer matches the TC measurement. This is because the heat transfer coefficient during this period (h_{amb}) is very small (25 W/m^2K). This drops the Biot number, internal temperature gradients subside, and the wheel behaves as a lumped system. The cooling rate in this regime increases in cases of less thermal mass. Since the thickness of the wheel near the thermocouple is only 2mm thick (owing to the hole drilled to place the thermocouple), the cooling rate near that region increases. This results in a faster rate of cooling measured by the thermocouple, relative to elsewhere in the wheel. Thus, the predictions are no longer expected to match the measurements.

VIII. Parametric Studies

The casting conditions during the melt-spinning process play a very important role in determining the quality of the product. Parametric studies have been performed to understand the effect of several process conditions on heat transfer, including casting speed, gap height, puddle length, superheat and interfacial depressions. To further validate the model, the first two zones of the five experimental cases were simulated according to the conditions in Table 1, with all other model parameters constant. Good agreement between the measured and predicted strip thickness is observed in each case.

A. Effect of casting speed (V_c): Casting speed is one of the most important factors that determines the thickness of the product. A thicker strip requires an increase in "residence time", or contact time in zone I, when the strip is beneath the puddle and in good contact with the wheel. Lowering casting speed increases this residence time and hence solidifies thicker strips. To isolate the effect of casting speed with constant puddle length, the process conditions for Case 43 (Table 1) were simulated for different casting speeds. Fig 14 quantifies the decrease in the strip thickness with increase in casting speed. Casting speeds ranging from 5-10 m/s were predicted to produce 0.25-0.16 mm thick strips. However, in reality, where flow rate is controlled (by maintaining the pressure head in the crucible), increasing speed decreases residence time, which increases the average heat transfer rate, (see Eq. (3)) and results in decreased puddle length. Specifically, doubling the casting speed halves the strip thickness for a constant flow rate. This makes the effect of casting speed on decreasing strip thickness more severe. The inner and outer wheel temperatures were observed to increase with casting speed due to increase in average heat transfer coefficients[40].

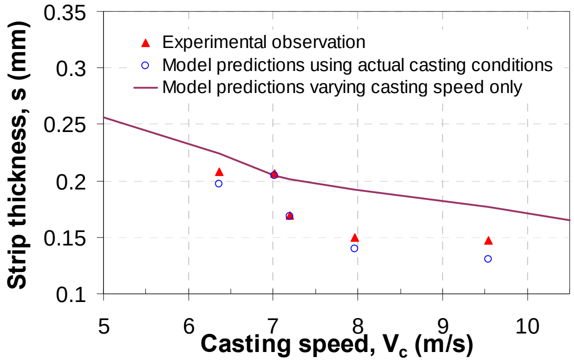

Figure 14: Effect of Casting speed on Strip thickness

B. Effect of gap height (G): Experimental observations indicate that strip thickness is directly related to gap height. As gap height also affects several other variables, its effect on strip thickness was investigated under four different sets of conditions.

1. *Experimental conditions:* The best model predictions of strip thickness for the actual experimental conditions, which already validate the model, are replotted as a function of gap height in Fig 15. The trend is very rough, owing mainly to changes in casting speed.

2. Varying PL=f(G) only: Transient measurements from all five cases were plotted[40] to reveal a trend in the puddle length variation with gap height. A curve fit to describe this variation is given by:

$$PL = 28.915G^2 - 21.314G + 14.385 \qquad (14)$$

Employing this relation to choose the puddle length, the effect of gap height on strip thickness was re-plotted, keeping all other conditions the same as standard Case 43. As expected, the strip thickness decreases with gap height, due to less residence time in zone I from the shorter puddle length. Fig 15 shows a sharp decrease in strip thickness for a gap height dropping until 0.61 mm, with more gradual drop for further gap reduction. This reflects the parabolic trend where the slope of the puddle length drops with decreasing gap height[40].

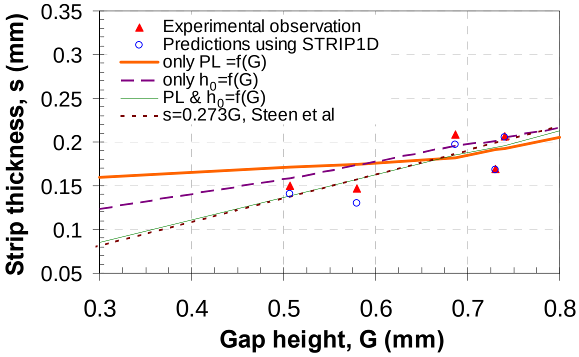

Figure 15: Effect of Gap height on Strip thickness

3. Varying h_0=f(G) only: To isolate the effect of gap height due to dropping the interfacial heat transfer coefficient, all conditions including puddle length were kept the same as that of Case 43, except for the relation (4). Fig 15 shows that strip thickness naturally drops with decreasing gap for this condition, due to the accompanying drop in heat transfer rate. For a gap height of 0.74, this condition is equivalent to simulating Case 43, so the line intersects the prediction for this experimental case. The drop in thickness is more severe than the previous condition, showing that the heat transfer effect of gap is more important than its effect on puddle length.

4. Varying PL=f(G) and h_0=f(G): This most realistic case includes both effects of gap height from the previous two conditions to study the combined effects of the interfacial heat transfer coefficient and puddle length on strip thickness. As shown in Fig 15, these two consequences of decreasing gap greatly decrease the strip thickness. Furthermore, the drop in the strip thickness for this condition is more severe than either of the individual effects alone (sections VIII B1 and VIII B2) because the effects are additive.

The real effect of gap height on strip thickness can also be determined using mass balance[9, 32, 47], and used for further model validation. Rearranging the mass balance and Bernouli-relation between head and flow rate, Eq [5] from Carpenter and Steen[9], gives

$$s = a\left[\frac{2\Delta P}{\rho V_c^2}\right]^{0.5} G \qquad (15)$$

Further setting the constant a=1[31], and substituting the values for pressure head, ΔP, V_c, and density, ρ, from Case 43 gives

$$s = 0.273G \qquad (16)$$

These equations show that an increase in gap height allows the liquid flow rate to increase, which increases the strip thickness (other conditions constant). Plotting this relation as a function of gap height in Fig. 15 intersects with the experimental point for case 43, demonstrating the accuracy of this simple relation in predicting strip thickness. This relation also produces an almost exact match with the strip thickness line obtained with condition 4. These results validate the predictive ability of present model. The heat transfer model can predict strip thickness accurately only by including the effects of gap on both heat transfer coefficient and puddle length.

C. Effect of puddle length (PL): Puddle length refers to the length of the melt pool which characterizes the time spent by the strip in Zone I. The effect of puddle length on strip thickness is investigated for two different conditions.

1. Varying PL only: The effect of varying puddle length on strip thickness is plotted in Fig 16, with all other conditions kept standard (Case 43). As expected, a nearly-linear decrease in strip thickness with decreasing puddle length is observed, owing to the decrease in residence time in the liquid pool. This result also shows an accidental match with the rough trend in the experimental cases.

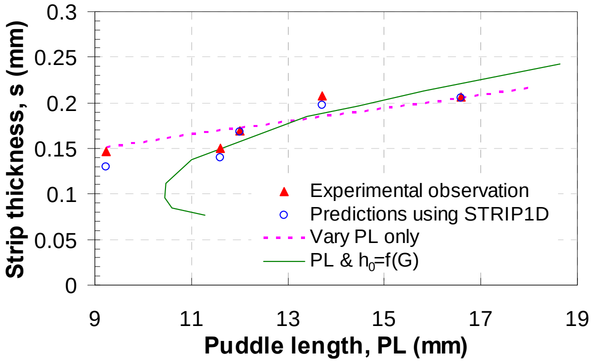

Figure 16: Effect of Puddle length on Strip thickness

2. Varying PL=f(G) and h_0=f(G): This more-realistic condition is re-plotted in Fig 16 from Fig 15 to present the typical expected effect of puddle length on strip thickness. It was observed in each of the five individual data sets that the puddle length in each cast initially decreases with time and decreasing gap height but later increases with further decrease in gap height towards the end of the cast. Initially, the decrease in gap height decreases the flow rate. This decreases the strip thickness and thereby shortens the puddle length, starting from the top right of the solid line in Fig 16. However, towards the end of cast, the smaller gap height lowers the heat transfer coefficient greatly, while only slightly decreasing the strip thickness. The net effect is that the puddle length must increase to allow time for this strip thickness to solidify. This effect is captured by the end of the solid line in Fig 16, where the puddle length increases for gap heights less than 0.37mm. The shortest puddle length is 10.45 mm[40]. This indicates that the puddle length is dictated by the heat transfer and the strip thickness, both of which are determined by the gap height.

D. Effect of super heat (ΔT): An increase in the superheat temperature tends to slow the solidification of the strip in the melt pool. This is captured in the model by increasing the superheat flux delivered at the liquid-solidifying mush interface. This increased superheat decreases the strip thickness, with other conditions (including puddle length) remaining constant. As superheat decreases towards zero, the strip thickness could eventually reach the gap height, causing a catastrophic freeze-up of the process. The effect can be prevented by increasing casting speed. In reality, decreasing superheat will shorten the puddle length, for a given flow rate and casting speed.

E. Effect of surface depressions: Surface depressions form where the meniscus first contacts the strip-wheel interface from several causes, discussed in Sections I and II. This section models the effects of two different types of wheel-side depressions on local heat transfer and thereby predicts the shape of the corresponding liquid-side surface depressions. Specifically, the model is applied to simulate longitudinal depressions caused by a linear ridge of interfacial boron nitride and transverse depressions due to rows of air pockets entrained at the meniscus / wheel interface.

1. Continuous BN-gap case: In order to quantify the effect of an interfacial BN ridge, several regions of the wheel were sprayed with a line of boron nitride (BN) deposits in the longitudinal direction (casting direction). After casting, longitudinal surface depressions formed on the liquid side of the opposite from the BN deposits. The 2-D model was applied to simulate and quantify this effect.

The depression shapes on both sides of the wheel were measured, as described in section III. The BN wheel-side ridge appeared as a line of dense dots along the casting direction. This was approximated as a continuous cylindrical trench along the strip. Fig 17 shows the domain, boundary conditions and mesh used to model the strip for this case.

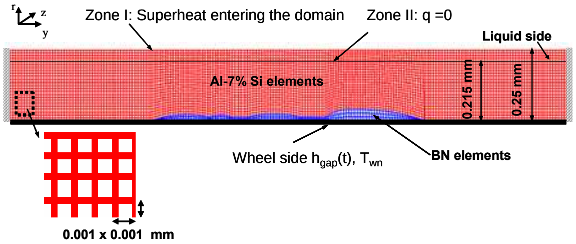

Figure 17: 2-D Domain, Boundary conditions & Mesh (BN case)

The elements comprising the wheel-side depression were assigned properties of BN. The contact resistance between the BN sprayed on the wheel and the strip has been neglected. The measured gap height for this sample was used to obtain the heat transfer coefficient from Eq. (4) at the strip wheel interface. The outer wheel temperatures obtained from the STRIP1D model, were used to complete this boundary condition. The superheat flux profile added at the top surface of the domain was adjusted until the solidification fronts obtained from the ABAQUS matched STRIP1D results, as shown in Fig 18. The model was then run in ABAQUS until the strip exited Zone I, using the measured puddle length to define the residence time.

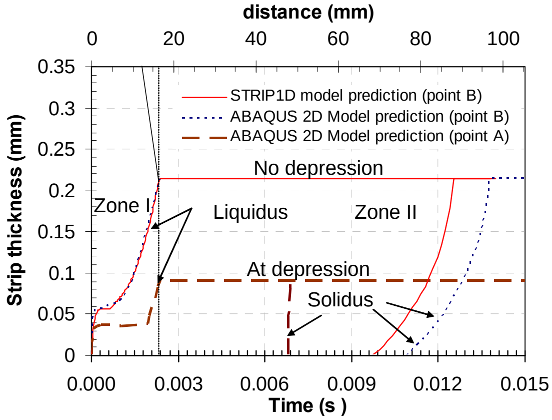

Figure 18: Solidification front growth profile (BN case)

The low conductivity of BN relative to Al-7%Si increases the thermal resistance across the BN-filled gap. This lowers the local solidification rate above the depression relative to the rest of the strip. This causes a corresponding depression on the liquid side of the strip. Fig 19 shows the temperature distribution through the thickness of the strip at the end of Zone I at two different locations: A (maximum depression depth) and B (right edge of the domain where heat transfer is 1-D). The temperature distribution through the strip thickness at point A indicates a very high temperature gradient within the BN depression, owing to its insulating ability. This produces higher temperatures in the strip just above. Temperature gradients through most of the strip (eg. point B) are very shallow, with maximum temperature differences of only ~25°C.

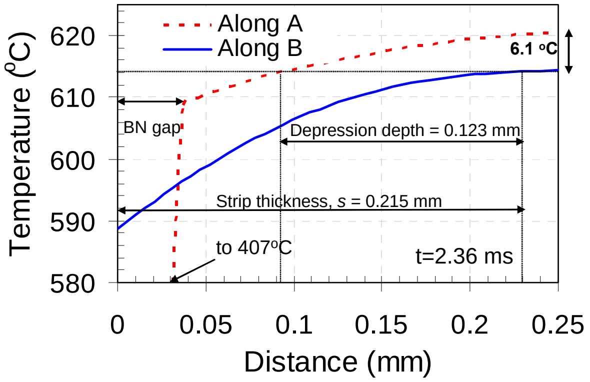

Figure 19: Strip temperature profiles at Zone I exit showing liquid-side depression depth (BN case)

Fig 19 also indicates the depth of the liquid-side depression. Intersecting the horizontal liquidus line (614^{o}C) with the temperature profiles indicates the strip thickness at points A and B. The difference is the depression depth of 123µm in this case. This is more than half of the 215µm total thickness at this location, indicating the substantial influence of the small BN ridge, which has a maximum thickness of less than 30µm. The complete depression shape (defined by $T > T_{liq}$) is revealed in the contour plot in Fig 20, which also shows a comparison with a micrograph of the sample. An excellent match is observed. The similar shape and difference in depth of only 2 µm strongly suggests that the model is reasonable. It should be noted, however, that the neglect of contact resistance between the BN and the strip may have cancelled the approximation of the BN deposits as a cylindrical trench, resulting in a near-perfect match.

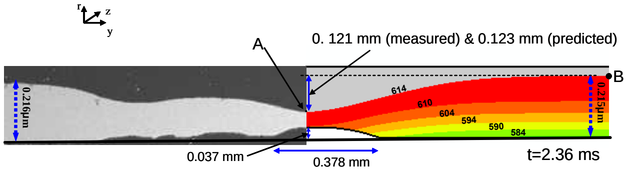

Figure 20 : Comparison between measured and predicted longitudinal depression profile at Zone I exit, (BN case)

Since only solid or mushy strip exits zone I, all of the liquid nodes ($T > T_{liq}$) were removed from the 2-D model. The simulation was then further run until the strip became fully solid, indicating the end of zone II. Fig 18 compares the solidification front growth of the liquidus and solidus for both the ABAQUS 2-D and STRIP1D models in zones I and II. The 2-D model predicts slightly higher temperatures and slower solidification because ABAQUS is unable to apply the superheat flux at the internal solidification front. The error is only about 3^{o}C, however, which validates both models.

It is interesting to note that solidification at the depression location (2-D model) is delayed while the strip is in zone I but is faster than the rest of the strip in zone II. In zone I, the low-conductivity gap naturally slows the local solidification. However once the strip enters zone II, there is no more liquid above the depression so the thin strip at the depression location can cool faster by conducting heat laterally .

2. Discontinuous air-gap case: The formation of the transverse surface depressions of the cross-stream pattern in Fig 1(a) was simulated with the 3-D model, assuming they are caused by the periodic rows of air pockets[9, 11] across the strip-wheel interface. Each row of air pockets is attributed to the continuous oscillation of the liquid pool which entraps air at the meniscus where the liquid metal and air contact together. These closely-spaced depressions represent a third time-scale of thickness variations along the strip. The model methodology was similar to that for the BN-gap case.

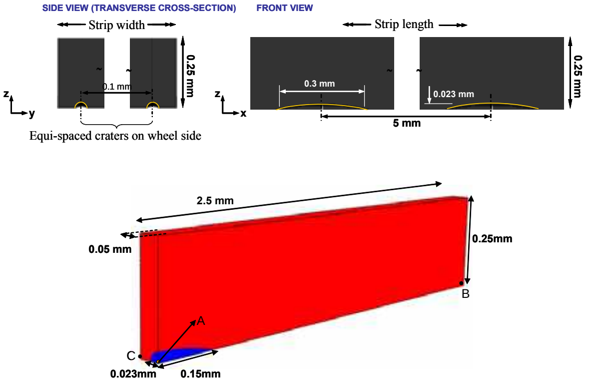

Figure 21: 3-D domain showing transverse depression geometry (Air gap case)

The boundary conditions were obtained by first running the STRIP1D model. Periodic symmetry was invoked in both directions, so the 3-D model domain needed to contain just one quarter of a single air pocket, as discussed in Section VI C, and shown in Fig 21 bottom. The air pockets are spaced every 0.1mm across the strip and are elongated in the casting direction with 5mm spacing (Fig 21 top). Table 1 gives the process conditions for this case. The strip- growth solidification front at a location far from the depression where the heat transfer is one-dimensional matched with that obtained from STRIP1D, which validates the 3-D model[40]. The liquid-side depression starts solidifying later, due to air pockets at the wheel-side. The air pockets themselves are seen to remain above the liquidus temperature for most of Zone I.

Fig 22 shows a 3-D view of the temperature contours in the domain to illustrate the predicted shape of the liquid side depression. The computed liquid-side depression depth is 50mm everywhere across the width. The predicted and measured depression shapes are compared in Fig 23 and the match is close.

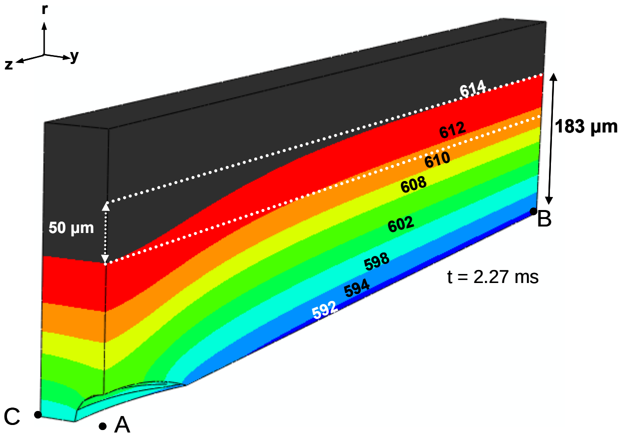

Figure 22: Temperature Contours through the strip at Zone I exit showing transverse depression (Air gap case)

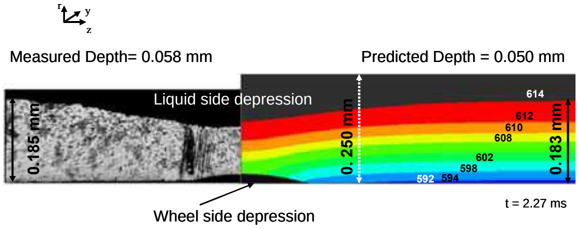

Figure 23: Comparison between measured & predicted transverse depression shapes at Zone I exit (Air gap case)

The small variations and uncertainty in the spacing of the small air pockets are responsible for the slight discrepancies. For the gas pocket size, shape and spacing studied here, the individual wheel-side depressions result in a continuous depression on the liquid side of the strip. If these wheel-side craters were deeper or spaced further apart, they would each produce an equivalent crater-shaped depression on the liquid side. Increase the depression depth further would deepen these depressions from both sides, eventually producing holes through the strip. This mechanism explains the formation of this type of surface defect has been observed in practice, as discussed in section I.

IX. Discussion

The relation between phenomena and controllable parameters in melt spinning and strip casting is presented schematically in Fig 24(a). This melt-spinning process studied in this work is "flow-rate controlled" with an unconstrained melt pool (puddle) whose length is governed by satisfying both strip thickness (mass balance) and heat transfer (heat balance). For a given nozzle geometry and width of the inlet, the flow rate is a direct function of both gap height and the pressure head exerted by the melt in the crucible. Applying a mass balance to relate the flow rate to the strip thickness at the puddle exit gives Eq (15), which quantifies how strip thickness depends directly on gap height and pressure and inversely with casting speed [9]. As shown in Fig. 24(a), it is proposed that a decrease in gap height also decreases the heat transfer coefficient, which together with the strip thickness determines puddle length. This means that any increase in heat transfer coefficient caused by an external process variable (such as substrate texture) for a given gap height produces strips with the same thickness, but requires the puddle length to become shorter in order to accommodate the faster solidification. As mentioned above, a dependency of the interfacial heat transfer coefficient on gap height has been incorporated into the model used in this study.

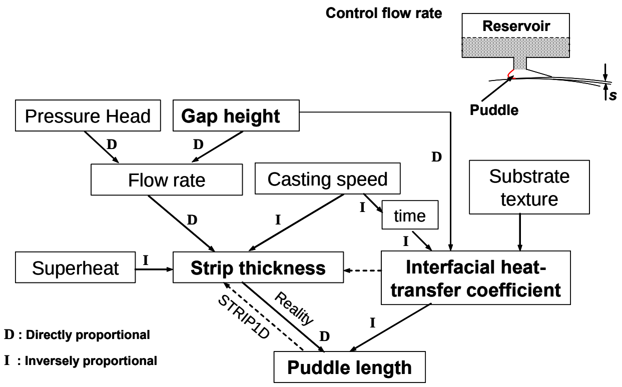

Figure 24(a): Relation between melt-spinning phenomena with unconstrained liquid pool (flow-rate controlled thickness)

Fig 24(b) shows a flow chart describing the phenomena of a single-roll or twin-roll strip-casting process where feedback control is used to maintain a constant liquid level in the melt pool reservoir. Since this maintains a constant puddle length contacting the strip, the interfacial heat transfer coefficient directly controls the strip thickness. Thus, this process is heat-transfer controlled. To satisfy mass balance, changes in strip thickness are accommodated by changing the liquid flow rate entering the reservoir using a flow control mechanism. The STRIP1D model has been developed using the same set of logical relations as this strip casting process, where the puddle length is treated as an input variable.

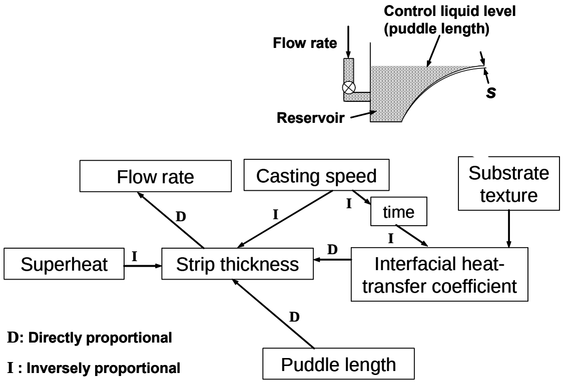

Figure 24(b): Relation between phenomena in constrained liquid pool strip-casting (heat transfer controlled thickness)

In a real melt-spinning process, puddle length is determined by the strip thickness and heat transfer, which are both determined by the gap height. These two effects of gap height variations are simultaneously responsible for the strip thickness variations observed in two different time scales. When this STRIP1D model is used to simulate the melt spinning process, the puddle length is treated as an input variable, which together with the heat transfer coefficient control the strip thickness (see dotted arrows in Fig 24(a)). Because heat balance and mass balance must both be satisfied, using the heat transfer model to simulate this process and accurately predict strip thickness from a given measured puddle length is equivalent to predicting the puddle length given a measured thickness. Thus, use of the STRIP1D heat-transfer model is valid. The results in Section VIII C have unorthodox presentation, however, in the sense that they appear to present the effect of puddle length on strip thickness. These results should be interpreted with puddle length (X axis) as the dependent variable.

In contrast to the melt spinning process, an increase in heat transfer coefficient directly increases the strip thickness in the strip casting process. This is because the constant liquid level fixes the puddle length so the process is not flow-rate controlled but heat-transfer controlled. For this reason, any slight change in heat transfer coefficient due to external factors, results in the formation of strip with non-uniform thickness. Changing the control variable in this process to allow the puddle length to adjust could greatly improve the consistency of strip thickness and quality in these processes.

X. Proposed Mechanism

A mechanism for solidification and the formation of transverse wavy depressions on the strip surface in the melt-spinning process has been developed based on this work. These steps are consistent with, and build upon the mechanism proposed by Steen and coworkers[6].

- The gap height and pressure head exerted by the melt in the crucible determine the flow rate of the liquid entering the melt pool. The flow rate increases with gap height due to the drop in flow resistance and with pressure head from the Bernoulli relations.
- Time-varying flow in the melt pool causes periodic oscillations of the meniscus, which continuously moves the upstream meniscus upstream and downstream along the wheel surface. The oscillation frequency increases with decreasing melt pool volume, so decreasing gap size causes more oscillations. .
- The upstream movement of the upstream meniscus captures air pockets at the wheel-meniscus contact interface. If capture occurs at the same instant during the meniscus oscillation, the gas pockets will form a discontinuous wavy line with the same shape as the melt pool meniscus at that instant.
- As metal solidifies around these pockets, they form wheel-side surface depressions that move with the strip through the melt pool at the wheel speed.
- The gas pockets retard heat transfer locally, which causes an equivalent liquid-side surface depression with the same shape. The depth of the liquid-side depressions grows with time, according to conduction within the strip. If the gas pockets are they aligned, then the depressions can merge into continuous lines, such as the cross-stream pattern.
- The pitch of the resulting defects naturally has the same frequency as the meniscus oscillation.
- With increasing time, thermal expansion of the heating wheel causes the gap height between the nozzle and the wheel surface to gradually decrease throughout the cast. Superimposed within each wheel rotation cycle, local variations in gap are caused by the slightly oblong shape of the wheel. Superimposed on these variations are the meniscus oscillations that are responsible for the third time scale of thickness variations.
- The decreasing gap height, and its accompanying higher frequency of menisci oscillations, and increased number of air pockets captured, causes a decrease in the average contact area between the liquid and wheel surface. This decreases the interfacial heat transfer coefficient.
- The decrease in gap height is also responsible for a decrease in flow rate which decreases the strip thickness to satisfy mass balance. Increasing casting speed would cause the same effects.
- Liquid in the melt pool remains until the strip thickness has solidified, which dictates the end of the puddle.

XI. Conclusions

This paper presents simple, yet accurate numerical models of the planar-flow melt-spinning process for Al-7%Si alloys on copper wheels: STRIP1D. The models include a realistic treatment of fluid flow and heat transfer in the melt pool, coupled with transient heat transfer and solidification of the strip and transient heat conduction within the wheel. Simultaneous predictions of transient strip thickness, SDAS, cooling rate, strip surface temperature and transient wheel temperature have been validated using experimental data measured at Cornell and excellent agreement has been observed. Two- and three-dimensional transient heat-transfer models of the planar-flow melt-spinning process have been developed using ABAQUS and validated with STRIP1D. The effect of process conditions including casting speed, puddle length, gap height, superheat and interfacial gaps on the heat-transfer occurring during this process have been investigated using these models. A method to quantify the surface depressions observed in melt spinning has been developed and validated using experimental measurements which reveals the mechanism of their occurrence. The following conclusions arise from this study.

- The superheat-flux method developed has been validated using multi-dimensional transient heat transfer models.
- Heat transfer across the wheel-strip interface governs solidification in the strip and heat transfer to the wheel. A new function for interfacial heat transfer coefficient h_{gap} is proposed: after a short time t_0 (0.1 ms) of constant (h_0) it decreases with time by:

$$h_{gap} = \begin{cases} h_0 & t \le 10^{-4} \\ h_0\left(\dfrac{10^{-4}}{t}\right)^{\frac{1}{3}} & t_{\det ach} > t > 10^{-4} \end{cases}$$

- In addition to controlling flow rate, and thereby strip thickness, a decrease in gap height seems also to decrease the interfacial heat transfer coefficient, perhaps due to increasing the oscillations in the puddle:

  $$h_0 = 225G$$

- Strip solidification depends greatly on residence time. As the contact time in zone I increases, the strip thickness increases.
- The observed non-classical strip growth profile for different solid fractions is steep with similar steep temperature contours almost parallel to each other. Also, the strip is mushy even after it enters Zone II and rapidly becomes fully solid near the end of Zone II.
- Parametric studies investigating the effects of various process variables; casting speed, gap height, puddle length, superheat and interfacial depressions on heat transfer have been determined.
- The gap height controls both the strip thickness and the heat transfer from the strip to the wheel, which together determine the puddle length.
- For all other conditions kept the same, an increase in superheat decreases the strip thickness because more heat enters the solidifying strip. If the superheat is very low, the strip might start solidifying at the nozzle resulting in freeze-up.
- Interfacial depressions on the wheel side of the strip interfere with the heat transfer to the wheel and decrease the local solidification rate resulting in an equivalent corresponding depression on the liquid side of the strip.
- The melt-spinning process is flow-rate controlled unlike the strip-casting process, which is heat-transfer controlled where the flow rate is controlled by thickness.
- Together, the STRIP1D and ABAQUS models comprise a powerful tool to study these processes. This paper explains the variations in the strip thickness observed in three different time / length scales.
    1. Thickness generally decreases with time during the entire cast, due mainly to decreasing gap height as the wheel expands, and also due to wheel heat-up.
    2. Thickness variations with the frequency of the wheel rotation are caused by gap variations due to slightly non-circular wheel shape.
    3. Small, closely-spaced transverse depressions occur due to the entrapment of air at the strip-wheel interface, owing to oscillation of the melt pool menisci. They can be predicted using a 3-D model that matches experimental measurements.

Acknowledgements

This project was done with the support of National Science Foundation (NSF), Grant # DMI 04-04-23794 and the Continuous Casting Consortium at UIUC. The authors wish to thank Professor Paul Steen and graduate students, Cormac J. Byrne, Eric A. Theisen and Miachel J. Davis at Cornell University for providing the experimental measurements from their pilot caster, the Center for Microanalysis of Materials partially supported by the U.S. Department of Energy under grant DEFG02-91-ER4543, James Mabon for helping with experimental measurements to obtain micrographs of sample, Joydeep Sengupta for initial research on the project and Rajneesh Chaudhary for helping with fluid-flow simulations.

References

1. H. H. Liebermann, "Ribbon-Substrate Adhesion Dynamics in Chill Block Melt-Spinning Processes", *Metall. Mater. Trans. B,* vol. 15 (1) (1984), pp. 155-161.
2. R. E. Maringer, "Solidification on a Substrate", *Mater. Sci. Eng.,* vol. 98 (1988), pp. 13-20.
3. S.Kavesh, " Metallic Glasses", ASM, J. H. Gilman and H. J. Leamy, eds.,Metals Park, OH, 1978, pp. 36-73.
4. M. Bussmann, J. Mostaghimi, D. W. Kirk and J. W. Graydon, "A numerical study of steady flow and temperature fields within a melt spinning puddle", *Int. J. Heat Mass Transfer,* vol. 45 (19) (2002), pp. 3997-4010.
5. J. K. Carpenter and P. H. Steen, "Heat transfer and solidification in planar-flow melt-spinning: High wheelspeeds", *Int. J. Heat Mass Transfer,* vol. 40 (9) (1997), pp. 1993-2007.
6. C. J. Byrne, E. A. Theisen, B. L. Reed and P. H. Steen, "Capillary puddle vibrations linked to casting-defect formation in planar-flow melt spinning", *Metall. Mater. Trans. B,* vol. 37 (3) (2006), pp. 445-456.
7. T.J.Praisner, "Experimental study of process behavior in planar flow melt spinning", *Metall. Mater. Trans. B,* vol. 26 (1995), pp. 1199-208.
8. J. S. J. Chen, R. C. Ren and A. A. Tseng, "Interface Heat-Transfer in Metal Casting on a Moving Substrate", *J.Mater. Proc. Manufac. Sci.,* vol. 3 (4) (1995), pp. 373-386.
9. J. K. Carpenter and P. H. Steen, "Planar-Flow Spin-Casting of Molten Metals - Process Behavior", *Journal of Materials Science,* vol. 27 (1) (1992), pp. 215-225.
10. J. P. Papai and C. E. Mobley, "Int. Symp. on Casting of Near Net Shape Products", TMS, Y.Sahai, J.E.Battles, R.S.Carbonara and C.E.Mobley, eds.,Warrendale, PA, 1988, pp. 79-90.
11. S. C. Huang and H. C. Fiedler, "Effects of Wheel Surface Conditionson on Casting of Amorphous Metal Ribbons", *Metall. Mater. Trans. B,* vol. 12 (6) (1981), pp. 1107-1112.
12. P. H. Steen and A. H. Hirsa, "New Technologies for the Environment: Environmentally Benign Manufacturing – Casting by design", (2002).
13. P.H. Steen, B.G. Thomas and S. Baker, "Collaborative Research: Contacting and Solidification in Casting-by-Design", (2005), vol. MPM # DMI0423791, pp. T/BGT/1-24.
14. P. H. Steen, U.S Patent 7,082,986 2006.

15. C. J. Byrne, S. J. Weinstein and P. H. Steen, "Capillary stability limits for liquid metal in melt spinning", *Chem. Eng. Sci,* vol. 61 (24) (2006), pp. 8004-8009.
16. G. Li and B. G. Thomas, "Transient Thermal Model of the Continuous Single-Wheel Thin-Strip Casting Process", *Metall. Mater. Trans. B,* vol. 27B (3) (1996), pp. 509-525.
17. C.A. Muojekwu, I.V. Samarasekera and J.K. Brimacombe, "Heat Transfer and Microstructure during the Early Stages of Metal Solidification", *Metall. Mater. Trans. B,* vol. 26B (2) (1995), pp. 361-382.
18. P. H. Steen and C. Karcher, "Fluid mechanics of spin casting of metals", *Annual Review of Fluid Mechanics,* vol. 29 (1997), pp. 373-397.
19. J. Kukura, K. Ford, A. Singh and P. H. Steen, "Measurement of heat transfer coefficient in planar flow casting", *Simul. Mat. Proc.: Theory, Methods, and Applications,* (1995), pp. 1153-57.
20. G. X. Wang and E. F. Matthys, "Numerical Modeling of Phase-Change and Heat-Transfer During Rapid Solidification Processes - Use of Control Volume Integrals with Element Subdivision", *Int. J. Heat and Mass Transfer,* vol. 35 (1) (1992), pp. 141-153.
21. N. H. Pryds and J. H. Hattel, "Numerical modelling of rapid solidification", *Modelling Simul.Mater. Sci. Eng.,* vol. 5 (5) (1997), pp. 451-472.
22. B.G. Thomas, "Modeling of Continuous-Casting Defects Related to Mold Fluid Flow", (2005), pp. 847-862.
23. J. Sengupta, B.G. Thomas, H.J. Shin, G.G. Lee and S.H. Kim, "Mechanism of Hook Formation during Continuous Casting of Ultra-low Carbon Steel Slabs", *Metall. Mater. Trans. A,* vol. 37 A (5) (2006), pp. 1597-1611.
24. S. N. Singh and K. E. Blazek, "Heat Transfer and Skin Formation in a Continuous Casting Mold as a Function of Steel Carbon Content", *J. Metals,* vol. 26 (1974), pp. 17-27.
25. M.S. Jenkins, B.G. Thomas, W.C. Chen and R.B. Mahapatra, "Investigation of strand surface defects using mold instrumentation and modelling", (1994), vol. 77, pp. 337-345, 82.
26. B.G. Thomas, D. Lui and B. Ho, "Effect of transverse depressions and oscillation marks on heat transfer in the continuous casting mold", (1997), pp. 117-142, 55.
27. J. Kubota, K. Okimoto, M. Suzuki, A. Shirayama and T. Masaoka, "Mechanism of Level Fluctuation and Mold Powder Catching in Slab Continuous Casting at High Speeds", (1990), vol. 3, pp. 356-363.
28. Y. Sasabe, S. Kubota, A. Koyama and H. Miki, "Real-time Expert System Applied to Mold Bath Level Control of Continuous Caster", *ISIJ Int.,* vol. 30 (2) (1990), pp. 136-141.
29. J. Legresey, Y. Brechet and P. Menet, "On The Origin of Short Wavelength Thickness Variations ofstrips in Melt Overflow Casting", *Scripta Mater.,* vol. 36 (12) (1997), pp. 1437-42.
30. C. J. Byrne, K. M. Aaron, S. P. Baker and P. H. Steen, "In situ manipulation of cooling rates during planar-flow melt spinning processing", *Mater. Sci. Eng. A,* vol. 459 (1-2) (2007), pp. 172-181.
31. P. H. Steen, E. A. Theisin and C. J. Byrne: Cornell University, Ithaca, NY, private communication with author, 2007.
32. P. H. Steen, B. L. Reed and M. B. Kahn, "Solidification-Induced Secondary Flows in Spin-Casting", *Inter. Dynamics of Convection and Solidification,* (2001), pp. 145-153.
33. X. Huang, B. G. Thomas and F. M. Najjar, "Modeling Superheat Removal during Continuous Casting of Steel Slabs", *Metall. Trans. B,* vol. 23B (6) (1992), pp. 339-356.
34. A. Sundararajan and B.G.Thomas, " Heat Transfer during Melt Spinning of Al-7%Si Alloy on a Cu-Be Wheel, Part I, Model Development and Validation", *Submitted to Metall. Mater. Trans. B.,* (2007).
35. *ABAQUS 6.7 Manual*, ABAQUS Inc.,Providence, RI, 2007.
36. *FLUENT6.1-Manual*, Fluent Inc.,Lebanon, New Hampshire, 2003.
37. G. Li and B.G. Thomas, "Transient Thermal Model of the Continuous Single-Wheel Thin-Strip Casting Process", *Metall. Mater. Trans.,* vol. 27B (3) (1996), pp. 509-525.
38. F. P. Incorpera and D. P. Dewitt: *Fundamentals of Heat and Mass Transfer*, 5 ed., John Wiley & sons, Hoboken, NJ, 2002.
39. J. Blumm, J. B. Henderson and L. Hagemann, "Measurement of thermophysical properties of an aluminum-silicon casting alloy in the solid and molten regions", ECTP, (1998), vol. 30, pp. 153-57.
40. A. Sundararajan and B. G. Thomas, " Heat Transfer during Melt Spinning of Al-7%Si Alloy on a Cu-Be Wheel, Part II, Parametric Studies and Modeling Surface Defects", *Submitted to Metall. Mater. Trans. B.,* (2007).
41. P. H. Steen, E. A. Theisen and C. J. Byrne: Cornell University, Ithaca, NY, private communication with author, 2007.
42. J. S. J. Chen, "Numerical modeling of a spin-casting process", ASME, (1996), vol. 4, p. 345.
43. M. Bamberger, B.Z. Weiss and M.M. Stuperl, *Mater. Sci. and Tech.,* vol. 3 (2) (1987), pp. 49-56.
44. J.E.Spinelli, M.D.Peres and A.Garcia, "Thermosolutal convective effects on dendritic array spacings in downward transient directional solidification of Al-Si alloys", *J. alloys and compounds,* vol. 403 (2005), p. 228.
45. I. Jimbo and A. Cramb, "The density of liquid iron-carbon alloys", *Metall. Mater. Trans. B,* vol. 24B (1993), pp. 5-10.
46. B. G. Thomas, J. T. Parkman and T. Chandra, "Thermec 97 Int. Conf. on Thermomechanical Processing of Steel and Other Materials", vol. 2, TMS,Wollongong, Australia, 1997, pp. 2279-2285.
47. P. H. Steen and T. Ibraki, "Melt Spinning, Strip Casting and Slab Casting", TMS, E. F. Matthys and W. G. Truckner, eds.,Warrandale, PA, 1996, pp. 159-171.

Name	**Validation Case**	**Case 43 (standard)**	**BN Case**	**Air pocket Case**
G = Gap height: (mm)	1.5	0.74	0.78	0.63
PL = Puddle length (mm)	23. 3	16.6	16.6	20.1
Zone II length (mm)	0	77.9	79.5	63.7
V_c = Wheel speed (linear) (m/s)	6.23	7.02	7.02	8.85
ΔT_s = Superheat: (K)	100	100	100	100
t_1 = Zone I contact time (ms):	3.74	2.36	2.36	2.27
h_0 = Interfacial heat transfer coefficient (kW/m^{2}K)	170	166.5	175.5	141.7
s = Strip thickness (mm)	0.233	0.206	0.215	0.183
Angles θ_1, θ_2 (^{o})	(4.39,0)	(3.13,14.7)	(3.13,15)	(3.13,12)

Table 1 : Process conditions for different cases